Research Square

Preprints are preliminary reports that have not undergone peer review.
They should not be considered conclusive, used to inform clinical practice,
or referenced by the media as validated information.

A hydrogen-dependent porosity-thresholds GTN model for coupled hydrogen transport and ductile fracture

Diego F. B. Sarzosa
dsarzosa@usp.br
Universidade de São Paulo
Sarnath Thoudam
Universidade de São Paulo
Mohsen Saneian
Universidade de São Paulo
Daniel C. Ferreira
Petrobras (Brazil)

Research Article

Keywords: Hydrogen-assisted fracture, GTN model, Hydrogen diffusion, Critical porosity, Void coalescence

Posted Date: November 24th, 2026

DOI: https://doi.org/10.21203/rs.3.rs-11679051/v1

License: This work is licensed under a Creative Commons Attribution 4.0 International License.
Read Full License

Additional Declarations: No competing interests reported.

A hydrogen-dependent porosity-thresholds GTN model for coupled hydrogen transport and ductile fracture

Mohsen Saneian[a], Sarnath Thoudam[a], Daniel C. Ferreria[b], Diego F.B. Sarzosa[a,*]

[a] *Department of Naval Architecture and Ocean Engineering, Universidade de São Paulo, São Paulo, Brazil*

[b] *Petrobras, Cenpes, Rio de Janeiro, Brazil*

Abstract

Predicting hydrogen-assisted ductile fracture requires accounting for interactions among hydrogen transport, plastic deformation, and void evolution. This study proposes a modified Gurson–Tvergaard–Needleman (GTN) model in which hydrogen affects the critical and final porosities governing void coalescence and material failure. Unlike existing approaches that modify void nucleation or growth, the proposed formulation retains the conventional GTN evolution laws and introduces hydrogen degradation through concentration-dependent porosity thresholds. Implemented in Abaqus/Standard using UMAT, UMATHT, and URDFIL, the framework couples hydrogen diffusion, trapping, stress-assisted transport, and ductile damage. The transport formulation is verified against reference crack-tip hydrogen distributions. Its predictive performance is evaluated against experimental tensile results for smooth and notched API 5L X70 steel specimens under different constraint levels and hydrogen concentrations. The model captures the overall hydrogen-induced reduction in deformation capacity, although it predicts premature softening for some geometries. Comparison with an independently calibrated Thomason-based formulation reveals distinct porosity evolution and plastic-work partitioning, despite similar macroscopic degradation trends. These findings show that hydrogen-assisted ductile failure can be represented through reduced resistance to void coalescence and subsequent deformation, without explicitly accelerating conventional void nucleation and growth. For academic and research purposes, the modified FORTRAN codes and accompanying example files are freely available at https://sites.usp.br/namef/vumat-umat/.

*Corresponding authors. Email address: dsarzosa@usp.br

Keywords: Hydrogen-assisted fracture; GTN model; Hydrogen diffusion; Critical porosity; Void coalescence

1. Introduction

According to Brazil's National Low-Carbon Hydrogen Policy, hydrogen is expected to play an important role as a vector for the energy transition across sectors of the Brazilian economy [1]. Therefore, repurposing existing natural-gas pipelines offers a promising alternative to constructing entirely new hydrogen transmission infrastructure [2]. Nevertheless, the use of conventional steel pipelines for hydrogen transport raises important structural-integrity concerns due to their susceptibility to hydrogen embrittlement (HE) [3]. Hydrogen exposure can adversely affect the mechanical and fracture response of pipeline steels, including their stress–strain behaviour, fracture resistance, and fatigue performance [4]. Hydrogen exposure can lead to significant reductions in ductility and fracture toughness, raising important concerns regarding the structural integrity of components operating in hydrogen environments [5]. Several mechanisms, including hydrogen-enhanced localised plasticity (HELP) and hydrogen-enhanced decohesion (HEDE), have been proposed, while increasing evidence suggests that hydrogen-assisted fracture may result from the interaction of multiple mechanisms rather than a single universal mechanism [6].

Accurate fracture prediction is essential for evaluating the structural integrity and remaining load-carrying capacity of engineering components [7]. Computational damage and fracture models provide an efficient alternative or complement to extensive experimental testing, allowing the initiation and evolution of material degradation to be investigated under complex geometries, stress states, and loading conditions [8]. Such numerical approaches are particularly valuable for hydrogen-assisted fracture, where the interaction between hydrogen transport, plastic deformation, and material damage must be considered simultaneously [9]. Nevertheless, reliable numerical prediction of hydrogen embrittlement remains challenging because of the strong coupling between hydrogen diffusion, trapping, mechanical fields, and fracture processes [10, 11].

The Gurson model [12] provides a micromechanical framework for describing the influence of spherical void growth on the constitutive response of porous materials. Since its introduction, several modifications have been proposed to extend its capability for predicting different stages and conditions

of ductile fracture. Chu and Needleman [13] incorporated void nucleation mechanisms controlled by local stress or accumulated plastic strain through a two-parameter nucleation formulation. Tvergaard [14] subsequently introduced additional parameters into the Gurson yield function to improve the representation of strain-hardening effects and interactions between neighbouring voids. The framework was further generalised by Gologanu et al. [15, 16] to account for non-spherical void geometries in ductile metals. To represent the final stage of ductile failure, Tvergaard and Needleman [17] incorporated void coalescence by modifying the effective void volume fraction entering the yield criterion. These developments resulted in what is commonly known as the Gurson–Tvergaard–Needleman (GTN) model, which has become a widely adopted micromechanical framework for describing the successive processes of void nucleation, growth, and coalescence leading to ductile fracture [18]. Moreover, it has been successfully applied to predict ductile fracture for notched and cracked fracture samples with different geometries and crack tip constraint levels [19, 20].

Hydrogen exposure has been shown to reduce the tensile ductility of stainless steel and to accelerate void nucleation and void-sheet formation by enhancing the localisation of shear deformation [21]. Despite such experimental evidence, the numerical representation of hydrogen embrittlement remains challenging [22]. Yu et al. [23] presented an early attempt to represent the hydrogen-enhanced localised plasticity (HELP) mechanism within the Gurson framework using unit-cell simulations. Hydrogen-induced degradation was introduced by accelerating void growth through a linear function of the local hydrogen concentration. This concept was subsequently extended by Depraetere et al. [24], who considered both HELP and hydrogen-enhanced strain-induced vacancy (HESIV) mechanisms by allowing the local hydrogen content to influence void growth, nucleation, and coalescence. Deng et al. [25] developed a GTN-based model for the mechanical response and failure of hydrogenated Zr-4 cladding, accounting for dissolved hydrogen and precipitated hydrides. Their model was implemented in ABAQUS to investigate the effects of hydrogen concentration, temperature, and oxide-layer thickness, as well as burst failure under LOCA conditions.

A different approach was proposed by Pinto et al. [26] to represent the hydrogen-enhanced decohesion (HEDE) mechanism. Their formulation combined a non-local GTN model with a hydrogen-dependent, principal-stress-based void nucleation criterion using mixed finite elements. The model reproduced the loading-rate dependence of damage initiation and propagation,

as well as the decrease in fracture strain at lower loading rates. However, its predictions were found to be strongly governed by the interaction among hydrogen diffusion, trapping kinetics, and damage evolution. More recently, Yu et al. [27] introduced a self-consistent void-based GTN framework for predicting the ductile-to-brittle transition (DBT). Grossi et al. [28] proposed a Bayesian optimization (BO) approach for efficient calibration of GTN parameters in hydrogen-charged MS1500 steel. Parameters identified from smooth tensile specimens were subsequently applied to V-notched specimens, demonstrating the applicability of the approach to more complex geometries. Patil et al. [29] developed a mesh-independent 3D finite element framework by coupling chemo-mechanical hydrogen transport with a non-local GTN model. The framework was designed to capture hydrogen-induced ductility reduction while providing damage regularisation and a modular basis for incorporating more advanced hydrogen embrittlement mechanisms.

Despite recent advances, a unified continuum description of plasticity-driven hydrogen embrittlement remains challenging. Existing GTN-based formulations generally incorporate hydrogen effects by modifying void nucleation, growth, coalescence, or a combination of these damage processes [30]. Among these approaches, Depraetere et al. [24] coupled hydrogen transport with the Complete Gurson Model (CGM) [31], allowing the local hydrogen concentration to accelerate different stages of void evolution and thereby represent HELP- and HESIV-related degradation. However, the direct influence of hydrogen on the critical condition governing the onset of void coalescence has received comparatively limited attention. Introducing a direct dependence of the critical porosity on the local lattice hydrogen concentration therefore provides an alternative approach for coupling hydrogen accumulation with the initiation of void coalescence and subsequent ductile fracture.

The experimental observations reported by Cauwels et al. [32] and Depraetere et al. [24] provide a physical basis for considering hydrogen-induced degradation through an earlier onset of ductile damage and void coalescence, while preserving the macroscopic plastic response of the matrix. Hydrogen charging had only a minor effect on the yield strength, tensile strength, and plastic anisotropy of API 5L X70 steel, whereas fracture strain was substantially reduced. Cauwels et al. further showed that hydrogen-assisted quasi-cleavage features (fisheyes) could develop before the maximum load was reached, and that the embrittlement index correlated with the area fraction of fisheyes for smooth and moderately notched specimens, although this

correlation broke down when delamination occurred. Complementary X-ray micro-CT observations by Depraetere et al. showed that hydrogen promotes damage initiation at lower strains and modifies void morphology, particularly through enhanced lateral growth, while the overall void-volume growth was not found to be systematically accelerated. Taken together, these observations do not provide a direct experimental measurement of the critical porosity, but they are consistent with the hypothesis that hydrogen can reduce the deformation threshold at which accelerated damage and coalescence begin. This motivates the present formulation, in which the effect of hydrogen is introduced through a hydrogen-dependent critical porosity while retaining the conventional GTN nucleation and scalar void-growth relations. The model is not proposed as a complete microscopic description of hydrogen embrittlement phenomena. Instead, it is a macrocopic description of an early coalescence threshold.

2. Methodology

2.1. Hydrogen difusion model

Hydrogen transport is modeled by a diffusion equation with trapping, following Oriani's equilibrium [33, 34]. Mass conservation of the diffusing species is expressed as

$$\frac{\partial C(x,t)}{\partial t} + \nabla \cdot \mathbf{J}(\mathbf{u}(x,t), C(x,t)) = r \qquad \text{in } \Omega \times [0,T], \tag{1}$$

where C denotes the total concentration field, $\mathbf{J}$ is the mass flux, and r represents volumetric sources or sinks. Note that the flux $\mathbf{J}$ may include both Fickian diffusion, which is proportional to ∇C and stress–assisted, proportional to $\nabla \sigma_H$, transport mechanisms. The total concentration C will be assumed to reside at two locations: normal interstitial lattice sites C_L (NILS) and trap sites C_T. For example, hydrogen is trapped in dislocations, carbides, and grain boundaries. The following boundary conditions complement hydrogen difusion problem: $C_L = \bar{c}$ on $\partial\Omega_c$, and $\mathbf{J} \cdot \mathbf{n} = \bar{q}$ on $\partial\Omega_q$, where $\partial\Omega_c$ and $\partial\Omega_q$ denote the boundaries with prescribed chemical concentration and flux, the outward unit normal vector is denoted by $\mathbf{n}$, and $\mathbf{J}$ is the flux vector. Likewise, initial time conditions should be defined for t =0 as $c(\mathbf{x}, 0) = c_0(\mathbf{x})$ in the solid body domain Ω.

The hydrogen flux vector $\mathbf{J}$ is proportional to the hydrogen concentration in lattice sites C_L and the gradient of the chemical potential μ_L of the hydrogen in the lattice sites. The proportionality factor is a function of the lattice

diffusivity coefficient D_L, which measures the mobility of the hydrogen in lattice sites. The first-order approximation of μ_L is given by [35]

$$\mu_L = \mu_L^0 + RTln\frac{C_L}{N_L} - V_H\sigma_H \tag{2}$$

where μ_L^0 is the reference chemical potential, N_L defines the number of lattice sites per unit volume, V_H is the partial molar volume of hydrogen in solid solution, and σ_H is the hydrostatic stress. the hydrogen flux is defined as

$$\boldsymbol{J} = -\frac{D_L C_L}{RT}\nabla\mu = -D_L\nabla C_L + \frac{D_L C_L V_H}{RT}\nabla\sigma_H, \tag{3}$$

Plug in back Equation 3 into Equation 1, the strong form equation governing hydrogen diffusion is:

$$\frac{\partial C_L}{\partial t} + \frac{\partial C_T}{\partial t} - \nabla\cdot(D_L\nabla C_L) + \nabla\cdot(\frac{D_L C_L \bar{V}_H}{RT}\nabla\sigma_h) = r \tag{4}$$

Equation 4 is solved by Abaqus after noting its analogy with the partial differential equation defining thermal transfer problems. The present approach uses coupled mechanical-thermal elements and an advanced thermal material model defined with a `UMATHT` subroutine to capture the spatial and temporal evolution of hydrogen concentration. Abaqus defines U as the internal thermal energy per unit mass, and the corresponding equivalent variable in the mass transport problem would be the total concentration of hydrogen $C = C_T + C_L$ ($U \equiv C$). For the mass-transport problem studied here, we set $r = 0$. Moreover, the temperature T in the heat analysis is chosen to be equivalent to the hydrogen content at the lattice sites C_L in the diffusion problem ($T \equiv C_L$).

2.2. Gurson–Tvergaard–Needleman damage model

The Gurson–Tvergaard–Needleman (GTN) model is adopted to describe ductile damage through the nucleation, growth, and coalescence of microscopic voids. The original Gurson model [12] was subsequently modified by Tvergaard and Needleman [14] to improve the description of void interaction and the final stage of ductile fracture. The GTN yield function can be expressed as [19]

$$\begin{aligned} \Phi &= \sigma_{\text{eq}} - (1-D)^{1/2}\,\sigma_y\left(\bar{\varepsilon}^p\right) = 0, \\ D &= 2q_1 f^* \cosh\left(\frac{3q_2\sigma_m}{2\sigma_y\left(\bar{\varepsilon}^p\right)}\right) - q_3(f^*)^2 \end{aligned} \tag{5}$$

where σ_{eq} is the von Mises equivalent stress, σ_m is the hydrostatic stress, σ_y denotes the current flow stress of the matrix material, and q_1, q_2, and q_3 are the Tvergaard parameters introduced to account for interactions between voids. At the microlevel, the material surrounding the cavities is considered elasto-plastic with isotropic hardening and being incompressible. At the mesolevel, the homogenised behaviour is elasto-plastic with a compressive response, i.e, a volume change different than zero. Note the reduction of material flow resistance as the porosity increases, controlled by the damage quantity D that is a highly nonlinear function of the porosity fraction and hydrostatic stress.

The variable f^* represents the modified void volume fraction used to describe the accelerated loss of load-carrying capacity after the onset of void coalescence. The modified void volume fraction is defined as

$$f^* = \begin{cases} f, & f \leq f_c, \\ f_c + \dfrac{f_u^* - f_c}{f_F - f_c}\left(f - f_c\right), & f > f_c, \end{cases} \tag{6}$$

where f is the current void volume fraction, f_c is the critical void volume fraction corresponding to the onset of void coalescence, and f_F denotes the void volume fraction associated with final fracture. The limiting value f_u^* is commonly expressed as

$$f_u^* = \frac{q_1 + \sqrt{q_1^2 - q_3}}{q_3}. \tag{7}$$

Prior to coalescence, the evolution of porosity results from both the growth of existing voids and the nucleation of new voids,

$$\dot{f} = \dot{f}_g + \dot{f}_n. \tag{8}$$

Assuming plastic incompressibility of the matrix material, void growth is related to the volumetric plastic strain rate according to

$$\dot{f}_g = (1 - f)\,\mathrm{tr}\left(\dot{\boldsymbol{\varepsilon}}^p\right). \tag{9}$$

Void nucleation is described using the strain-controlled formulation proposed by Chu and Needleman [13],

$$\dot{f}_n = A_N \dot{\bar{\varepsilon}}^p, \tag{10}$$

where $\bar{\varepsilon}^p$ is the equivalent plastic strain of the matrix and A_N follows a normal distribution,

$$A_N = \frac{f_N}{s_N\sqrt{2\pi}} \exp\left[-\frac{1}{2}\left(\frac{\bar{\varepsilon}^p - \varepsilon_N}{s_N}\right)^2\right], \tag{11}$$

in which f_N represents the volume fraction of nucleating particles, ε_N is the mean nucleation strain, and s_N is the corresponding standard deviation.

Accordingly, ductile fracture within the GTN framework develops sequentially through void nucleation, progressive void growth, and finally void coalescence. The parameter f_c is therefore particularly important because it determines the porosity level at which accelerated coalescence begins.

2.3. Hydrogen-assisted damage in the GTN framework

The classical GTN formulation does not explicitly account for the influence of hydrogen on the deformation and damage processes of the material. Several extensions have therefore been proposed in which the local hydrogen concentration is coupled to different stages of ductile damage evolution. In particular, Depraetere et al. [24] developed a fully coupled framework in which hydrogen may promote void growth, void nucleation, and void coalescence. These modifications were introduced to phenomenologically represent hydrogen-assisted mechanisms such as hydrogen-enhanced localised plasticity (HELP) and hydrogen-enhanced strain-induced vacancy formation (HESIV).

The influence of hydrogen on void growth and nucleation was introduced through concentration-dependent scaling factors. Considering contributions from lattice and trapped hydrogen, the corresponding evolution equations can be written as

$$\dot{f}_g^H = \dot{f}_g^0 \left(1 + k_{g,L}C_L + k_{g,T}C_T\right), \tag{12}$$

and

$$\dot{f}_n^H = \dot{f}_n^0 \left(1 + k_{n,L}C_L + k_{n,T}C_T\right), \tag{13}$$

where $\dot{f}_g^0$ and $\dot{f}_n^0$ denote the void growth and nucleation rates in the absence of hydrogen, respectively. C_L and C_T represent the lattice and trapped hydrogen concentrations, while $k_{g,L}$, $k_{g,T}$, $k_{n,L}$, and $k_{n,T}$ are degradation parameters that determine the sensitivity of the corresponding damage mechanisms to hydrogen [24].

In addition to modifying the evolution of porosity, Depraetere et al. [24] considered the effect of hydrogen on the mechanical resistance of the matrix material. Based on the HELP concept, the hydrogen-reduced matrix flow stress was defined using a piecewise softening relationship,

$$\bar{\sigma}_H(C_L) = \begin{cases} \left[1 + (\xi - 1)\dfrac{C_L}{C_L^0}\right]\bar{\sigma}, & \bar{\sigma}_H > \eta\bar{\sigma}, \\ \eta\bar{\sigma}, & \bar{\sigma}_H \leq \eta\bar{\sigma}, \end{cases} \tag{14}$$

where $\bar{\sigma}$ is the hydrogen-free matrix flow stress, $\bar{\sigma}_H$ is its hydrogen-dependent counterpart, ξ controls the magnitude of hydrogen-induced softening, and C_L^0 is the initial lattice hydrogen concentration. The parameter η defines the minimum retained fraction of the hydrogen-free flow stress.

An important aspect of this formulation is that Equation (14) was not directly substituted into the GTN yield function. Depraetere et al. argued that hydrogen-induced softening associated with HELP is highly localised in the intervoid ligament. Applying the same reduction to the matrix flow stress of the entire continuum material point would therefore represent global softening rather than the intended localised degradation. Consequently, the reduced flow stress $\bar{\sigma}_H$ was employed only within the Thomason coalescence criterion, thereby promoting an earlier onset of void coalescence without directly softening the complete GTN yield surface [24].

The above framework therefore introduces hydrogen effects through two different routes: modification of the porosity evolution through accelerated void growth and nucleation, and modification of the coalescence condition through hydrogen-dependent matrix softening. Although this provides considerable flexibility for representing different hydrogen-assisted mechanisms, some limitations remain. In particular, directly scaling the void growth rate changes the original micromechanical interpretation of f as the physical void volume fraction. Thus, f should be understood as a *numerical damage variable* controlling the material's load-bearing capacity. Since the conventional growth law follows from volume conservation, introducing an additional hydrogen-dependent multiplier means that this conservation basis is no longer strictly maintained [24]. Moreover, the additional degradation coefficients require calibration for the material and hydrogen conditions under consideration.

These observations provide the motivation for the alternative coupling strategy developed in the present work. Rather than directly accelerating the

evolution of porosity, the proposed formulation seeks to preserve the conventional void nucleation and growth laws while introducing the hydrogen effect through a material parameter governing the resistance to ductile damage. The details of this formulation are presented in the following subsection.

2.4. Proposed hydrogen-dependent critical porosity model

The hydrogen-assisted GTN formulations discussed in the previous section introduce hydrogen degradation by directly accelerating void growth or void nucleation, or by reducing the matrix flow stress entering the coalescence criterion [24]. In particular, multiplying the conventional void-growth rate by a hydrogen-dependent degradation factor changes the original micromechanical interpretation of the void volume fraction, since the classical growth term is derived from volume conservation. This limitation was also acknowledged by Depraetere et al. [24].

In the present work, an alternative coupling strategy is proposed. Rather than directly modifying the evolution of the void volume fraction, the conventional GTN equations governing void nucleation and growth are retained. The effect of hydrogen is instead introduced through the critical porosity, which defines the onset of accelerated void coalescence. Accordingly, hydrogen is assumed to reduce the material resistance to coalescence, such that the critical porosity becomes dependent on the local lattice hydrogen concentration. The proposed relationship is expressed as

$$f_c(C_L) = f_c^0 - \zeta_1 \left[1 - \exp\left(-\zeta_2 C_L\right)\right], \tag{15}$$

where f_c^0 denotes the critical porosity of the hydrogen-free material, while $f_c(C_L)$ represents the corresponding hydrogen-dependent critical porosity, which is treated as an *effective phenomenological parameter*. The parameters ζ_1 and ζ_2 govern the hydrogen-induced degradation. The parameter ζ_1 controls the maximum reduction in critical porosity, whereas ζ_2, with units of wppm^{-1}, controls its sensitivity to the local lattice hydrogen concentration. The condition $0 < \zeta_1 \leq f_c^0$ ensures that $f_c(C_L)$ remains non-negative. The proposed relationship satisfies the hydrogen-free condition, $f_c(0) = f_c^0$, and approaches the limiting value $f_c^0 - \zeta_1$ with increasing hydrogen concentration.

To account for the influence of hydrogen on the post-coalescence response, the ultimate void volume fraction is also assumed to decrease with increasing hydrogen concentration. This dependence is expressed as

$$f_f(C_L) = f_f^0 \exp\left(-\zeta_3 C_L\right), \tag{16}$$

where f_f^0 denotes the ultimate void volume fraction of the hydrogen-free material, while $f_f(C_L)$ represents its hydrogen-dependent value. The parameter ζ_3, with units of wppm^{-1}, controls the sensitivity of the ultimate void volume fraction to the local lattice hydrogen concentration. Equation 16 satisfies the hydrogen-free condition, $f_f(0) = f_f^0$, and progressively reduces the ultimate void volume fraction with increasing hydrogen concentration.

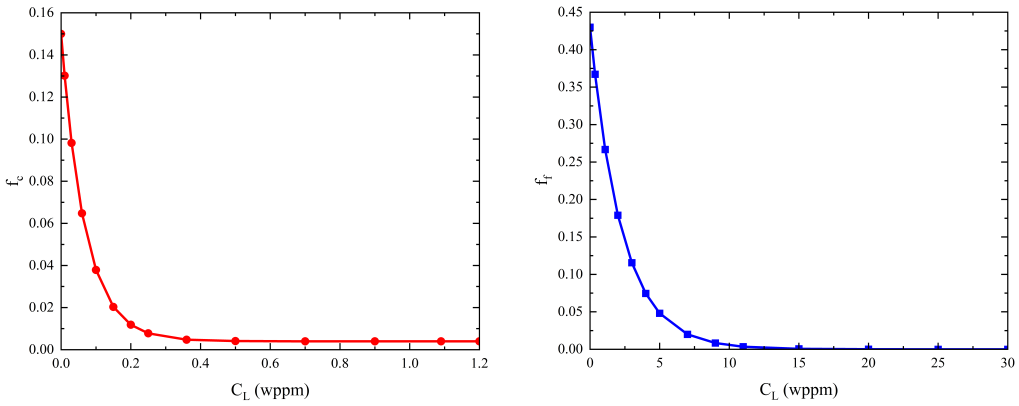


Figure 1: Hydrogen-dependent porosity parameters as a function of the local lattice hydrogen concentration C_L: (a) critical porosity $f_c(C_L)$; (b) ultimate void volume fraction $f_f(C_L)$.

Figure 1 illustrates the influence of the local lattice hydrogen concentration on the two porosity parameters introduced in the proposed model. As shown in Figure 1(a), the critical porosity f_c decreases rapidly with increasing C_L and progressively approaches its limiting value. This reduction causes the onset of accelerated void coalescence to occur at a lower porosity as the local hydrogen concentration increases. Similarly, Figure 1(b) shows a progressive reduction in the ultimate void volume fraction f_f with increasing C_L, thereby reducing the porosity level associated with final material failure. Consequently, the proposed formulation accounts for the influence of hydrogen on both the onset of void coalescence and the subsequent post-coalescence response.

An important feature of the proposed approach is that hydrogen does not directly multiply the void-growth or void-nucleation rates. The evolution of the physical void volume fraction therefore retains the conventional GTN formulation, while hydrogen modifies the porosity thresholds governing the

transition to accelerated coalescence and the subsequent loss of load-carrying capacity.

The proposed formulation also differs from the hydrogen-dependent coalescence treatment of Depraetere et al. [24]. Their approach employs a hydrogen-reduced matrix flow stress within the Thomason coalescence criterion, whereas the present model retains the hydrogen-free matrix constitutive response and introduces hydrogen degradation directly through the porosity parameters $f_c(C_L)$ and $f_f(C_L)$. This provides a simple phenomenological coupling between the evolving hydrogen field and the coalescence and failure stages of ductile fracture without directly modifying the conventional void nucleation and growth laws.

3. Numerical analysis

3.1. Verification of URDFIL and UMATHT routines

Prior to the coupled fracture simulations, the numerical implementation of the hydrogen transport formulation was verified using a modified boundary layer (MBL) model. The MBL configuration, shown in Figure 2, provides a convenient benchmark for evaluating stress-assisted hydrogen redistribution in the vicinity of a stationary crack, where strong hydrostatic stress gradients develop ahead of the crack tip [36].

The model consists of a circular domain containing a crack and subjected to plane-strain Mode-I loading [37]. A prescribed displacement field corresponding to the analytical crack-tip solution was imposed along the outer boundary. The applied displacement was defined by a stress intensity factor of $K_I = 89.2$ MPa$\sqrt{\text{m}}$. Although three-dimensional solid elements were employed in the present implementation, plane-strain conditions were reproduced using a single element layer through the thickness, together with appropriate out-of-plane symmetry constraints.

A uniform initial lattice hydrogen concentration, $C_{L,0}$, was assigned to the entire domain, while the same concentration was maintained at the outer boundary throughout the analysis. Hydrogen redistribution was subsequently calculated under the evolving crack-tip stress field. The normalised lattice and trapped hydrogen concentrations were evaluated along the ligament ahead of the crack tip as functions of the normalised distance R/b.

Figure 3 compares the predicted lattice hydrogen concentration, $C_L/C_{L,0}$, with the results of Krom et al. [35] at different loading times and at steady

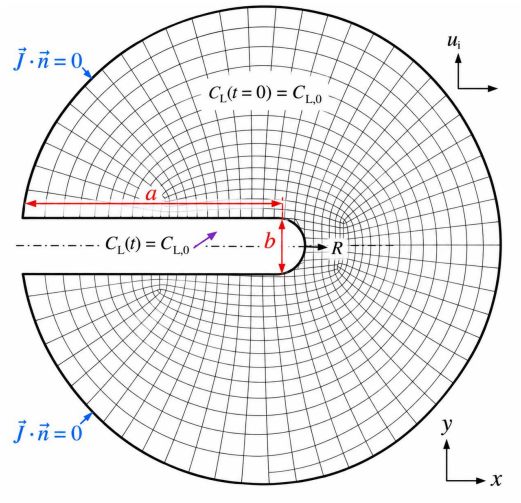


Figure 2: Modified boundary layer model and boundary conditions used for verification of the hydrogen transport formulation.

state. The evolution from an initial depletion near the crack tip to a pronounced hydrogen accumulation at longer times is well reproduced by the present model. Similarly, Figure 4 presents the normalised trapped hydrogen concentration, $C_T/C_{L,0}$, where close agreement with the reference results is obtained for both the transient and steady-state distributions. These comparisons verify the implementation of the hydrogen transport formulation prior to its application to the coupled hydrogen–GTN simulations.

3.2. FE implementation of the coupled hydrogen–GTN framework

The proposed constitutive framework was implemented in ABAQUS/Standard using the user subroutines UMAT, UMATHT, and URDFIL. UMAT is based on the source code developed by Zhang et al. [31] and is used to evaluate the mechanical response, including plastic deformation and void evolution. UMATHT is employed to solve the hydrogen transport problem through the heat-transfer analogy introduced previously. The variables required for coupling the mechanical and hydrogen transport formulations are transferred between the user subroutines through solution-dependent state variables and FORTRAN common blocks. In particular, the increment of equivalent plastic strain calculated in UMAT is made available to UMATHT for the evaluation of hydrogen trapping [38].

Stress-assisted hydrogen diffusion additionally depends on the spatial

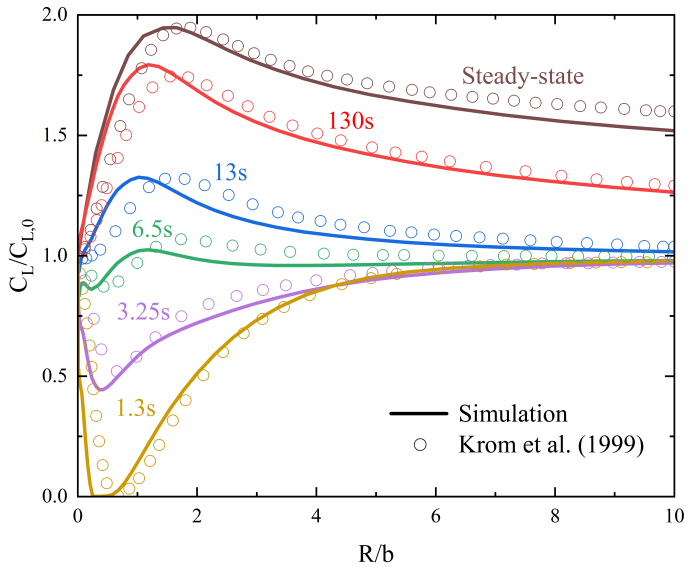


Figure 3: Comparison of the normalised lattice hydrogen concentration $C_L/C_{L,0}$ along the crack-tip ligament with the benchmark results of Krom et al. [35] at different loading times and at steady state.

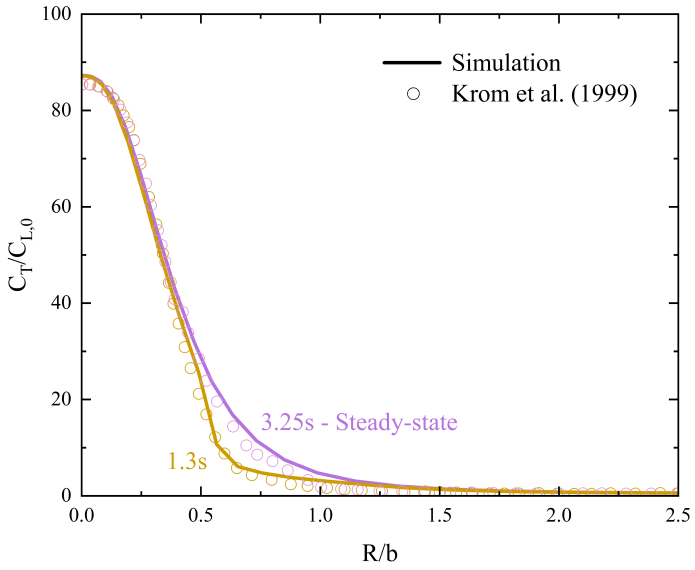


Figure 4: Comparison of the normalised trapped hydrogen concentration $C_T/C_{L,0}$ along the crack-tip ligament with the benchmark results of Krom et al. [35] at different loading times and at steady state.

gradient of hydrostatic stress, $\nabla\sigma_h$. Since this quantity is not directly available within UMATHT, it is numerically reconstructed using the URDFIL user subroutine. Three-dimensional eight-node coupled temperature–displacement elements (C3D8T) are employed in the present analyses. For each element, the hydrostatic stress field is reconstructed from its nodal values, and the corresponding gradient at each integration point is evaluated through differentiation of the finite element shape functions [39]. Accordingly,

$$\nabla\sigma_h = \begin{bmatrix} \displaystyle\sum_{i=1}^{8} \frac{\partial N_i}{\partial x}\sigma_{h,i}^N \\ \displaystyle\sum_{i=1}^{8} \frac{\partial N_i}{\partial y}\sigma_{h,i}^N \\ \displaystyle\sum_{i=1}^{8} \frac{\partial N_i}{\partial z}\sigma_{h,i}^N \end{bmatrix}, \tag{17}$$

where N_i denotes the shape function associated with node i and $\sigma_{h,i}^N$ is the corresponding nodal hydrostatic stress. The derivatives appearing in Equation (17) are transformed from the natural element coordinates (ξ, η, ζ) to the global coordinate system (x, y, z) according to

$$\begin{bmatrix} N_{i,x} \\ N_{i,y} \\ N_{i,z} \end{bmatrix} = \mathbf{J}^{-1} \begin{bmatrix} N_{i,\xi} \\ N_{i,\eta} \\ N_{i,\zeta} \end{bmatrix}, \tag{18}$$

in which $\mathbf{J}$ represents the element Jacobian,

$$\mathbf{J} = \begin{bmatrix} \displaystyle\sum_{i=1}^{8} N_{i,\xi}x_i & \displaystyle\sum_{i=1}^{8} N_{i,\xi}y_i & \displaystyle\sum_{i=1}^{8} N_{i,\xi}z_i \\ \displaystyle\sum_{i=1}^{8} N_{i,\eta}x_i & \displaystyle\sum_{i=1}^{8} N_{i,\eta}y_i & \displaystyle\sum_{i=1}^{8} N_{i,\eta}z_i \\ \displaystyle\sum_{i=1}^{8} N_{i,\zeta}x_i & \displaystyle\sum_{i=1}^{8} N_{i,\zeta}y_i & \displaystyle\sum_{i=1}^{8} N_{i,\zeta}z_i \end{bmatrix}, \tag{19}$$

where (x_i, y_i, z_i) are the current nodal coordinates. The use of nodal stresses for this reconstruction provides a continuous representation of the stress field

across adjacent elements and avoids directly differentiating integration-point quantities [40].

The `URDFIL` subroutine is used to compute the spatial gradient of the hydrostatic stress required by the stress-assisted hydrogen transport model. At the end of each converged increment, the subroutine `URDFIL` reads the Abaqus results file using the `DBFILE` utility and retrieves the element connectivity (record key 1900), current coordinates, and the stress invariants, including the hydrostatic pressure (SINV, record key 12). The average pressure field is recovered at the nodes from the available element results and subsequently interpolated within each element using its shape functions, allowing its spatial gradient to be evaluated from the nodal values. Since Abaqus defines the hydrostatic pressure as $p = -\frac{1}{3}\,\mathrm{tr}(\boldsymbol{\sigma})$, the hydrostatic stress is $\sigma_H = -p$, and therefore $\nabla\sigma_H = -\nabla p$. The resulting stress-gradient field is stored by `URDFIL` and made available in a common FORTRAN variable to the thermal constitutive routine UMATHT for evaluation of the stress-assisted contribution to the hydrogen flux. The Jacobian is updated during the analysis so that changes in element geometry associated with finite deformation are included in the gradient calculation. The element connectivity is automatically extracted from the FIL file during the first call, while the results are updated after each converged increment. The `LOVRWRT=1` option is used to overwrite the previous FIL data, avoiding unnecessary growth of the FIL results file.

A key feature of the present implementation is the automatic extraction of the element–node connectivity directly from the Abaqus `.fil` file. The connectivity information is stored in record key 1900, which is written before the default reading position used by `DBFILE(0,ARRAY,JRCD)`. Therefore, the file reading position must first be reset to the beginning using `DBFILE(2,ARRAY,JRCD)`. The `URDFIL` routine can then sequentially read the file and identify the records associated with key 1900, from which the element type, element number, and nodal connectivity are automatically obtained and stored. This procedure eliminates the need for a separately generated element–node connectivity file and makes the proposed implementation directly applicable to arbitrary meshes without modifying the connectivity data manually.

The sequence of the ABAQUS user routines determines the exchange of variables within the coupled solution. The plastic-strain information generated by UMAT can be transferred to the hydrogen calculation within the current increment, whereas the hydrostatic stress gradient evaluated through URDFIL becomes available after convergence and is therefore employed in

the following increment. Consequently, sufficiently small time increments are used to limit the numerical error associated with this one-increment delay. Through this procedure, deformation and damage modify the hydrogen distribution through plasticity-dependent trapping and stress-assisted diffusion, while the resulting local hydrogen concentration is simultaneously supplied to the hydrogen-dependent GTN constitutive relations.

4. Calibration and Validation of the Numerical Framework

4.1. Specimen models

The experimental data employed in this study were obtained from the tensile tests conducted by Depraetere et al. [41] on API 5L X70 pipeline steel [42]. The specimens were extracted along the longitudinal direction of the pipe and comprised a smooth geometry (R_∞) and three notched geometries with notch radii of 1.2, 2, and 6 mm, denoted as $R_{1.2}$, R_2, and R_6, respectively. These geometries provide different levels of mechanical constraint, with initial stress triaxialities of approximately 1.14, 0.89, 0.56, and 0.33 for $R_{1.2}$, R_2, R_6, and R_∞, respectively.

For the hydrogen-charged tests, the specimens were electrochemically precharged for six hours, resulting in an approximately uniform hydrogen content of 0.36wppm and 1.09wppm. Tensile testing was initiated approximately seven minutes after charging at a nominal strain rate of 2.5×10^{-4} s^{-1}. The experimental results generally showed increasing hydrogen embrittlement with increasing $C_{L,0}$ and stress triaxiality, except for the $R_{1.2}$ specimen at $C_{L,0} = 0.36$ wppm. The smooth specimens (R_∞) exhibited significantly less degradation than the notched specimens [43]. Due to the limited number of $R_{1.2}$ tests, a standard deviation could not be determined. The resulting experimental responses were used for calibration and validation of the proposed hydrogen–GTN framework.

Three-dimensional FE models were developed in ABAQUS/Standard to reproduce the uncharged and hydrogen-charged tensile tests. Owing to symmetry, only one-quarter of each specimen was modelled. A symmetry boundary condition was applied at one end of the model, while tensile loading was imposed at the opposite end. An additional symmetry condition was prescribed on the longitudinal symmetry surface of the quarter model, as shown in Figure 5. Based on the discretisation study reported by Depraetere et al. [24], an element size of 0.2 mm and a time increment of $\Delta t = 6$ s were

adopted in the present study. These values were shown to provide an appropriate balance between numerical convergence, accuracy, and computational efficiency for the coupled hydrogen-diffusion and damage simulations. For the hydrogen-free simulations, C3D8 elements were used, whereas C3D8T coupled temperature–displacement elements were employed for the hydrogen-charged simulations to account for the coupled mechanical and hydrogen-transport response. To reproduce the experimental loading conditions, the notched specimens were represented using a single notch and subjected to a strain rate of 1.25×10^{-4} s^{-1}, whereas the smooth specimen was loaded at a constant strain rate of 2.5×10^{-4} s^{-1}.

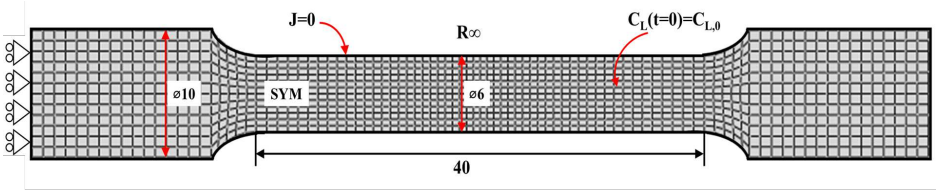
For the hydrogen-charged simulations, a uniform initial lattice hydrogen concentration $C_{L,0}$ was assigned throughout the specimen. A zero-flux condition, $J = 0$, was imposed on the external surfaces during mechanical loading, assuming negligible hydrogen loss over the duration of the test [44]. Hydrogen was subsequently allowed to redistribute within the specimen according to the coupled diffusion–trapping formulation [45].

In the present constitutive framework, the local lattice hydrogen concentration C_L is adopted as the hydrogen variable governing material degradation. Although the trapped hydrogen concentration C_T is evaluated as part of the diffusion–trapping analysis, its contribution is not introduced separately into the damage relations [46].

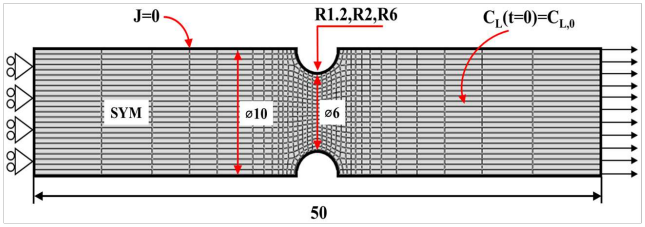
4.2. Material parameters

The mechanical response of the API 5L X70 steel was defined using the experimentally determined true stress–true plastic strain relationship reported in [43]. The corresponding flow curve was directly prescribed as the constitutive input for the present finite element simulations and is therefore not reproduced here. The material, GTN model, and hydrogen-transport parameters adopted in the simulations are summarised in Table 1.

The Tvergaard coefficients q_1, q_2, and q_3 were selected based on the unit-cell results of Faleskog et al. [47], considering the yield strength and strain-hardening characteristics of the investigated steel. The critical void volume fraction f_c, which governs the onset of void coalescence, is not included in Table 1, since it is determined separately through the calibration procedure described in the following section.



(a) Smooth round bar



(b) Notched round bar

Figure 5: Finite element models, geometries, mesh discretisation, and boundary conditions for (a) the smooth round-bar specimen and (b) the notched round-bar specimens with notch radii of $R = 6$, 2, and 1.2 mm.

Table 1: Material, GTN model, and hydrogen-transport parameters.

Material parameters								
			E (MPa)	ν	σ_y (MPa)	n		
			207000	0.30	455	0.12		
GTN model parameters								
q_1	q_2	q_3	α	ε_N	S_N	f_0	f_N	f_f^0
1.42	0.96	2.0164	1.0	0.578	0.5	0.0034	0.031	0.43
Hydrogen-transport parameters								
			D_L (mm^2/s)	E_B (kJ/mol)	N_L (m^{-3})	T (K)		
			4.5×10^{-4}	-30	8.47×10^{28}	300		

4.2.1. Calibration of material parameters

The calibration was first performed under hydrogen-free conditions to determine the critical porosity f_c, which controls the onset of void coalescence in the GTN formulation. The R_6 specimen was selected for this purpose because its high stress triaxiality provides a pronounced damage and coalescence response [48]. During the calibration, all other material and GTN parameters were kept fixed at the values reported in Table 1, and only f_c was varied.

A one-dimensional parameter search was carried out by progressively varying f_c within its physically admissible range,

$$f_0 < f_c < f_f^0 \tag{20}$$

A coarse parameter sweep was initially employed to identify the region providing the closest agreement with the experiment, followed by progressively finer variations of f_c within this interval.

For each candidate value of f_c, the numerical response was compared with the experimental R_6 curve in terms of the normalised load F/A_0 as a function of the true strain $\ln(A_0/A)$. The quality of the agreement can be expressed through the root-mean-square error (RMSE) [49],

$$\mathrm{RMSE}(f_c) = \sqrt{\frac{1}{N}\sum_{i=1}^{N}\left[\left(\frac{F}{A_0}\right)_i^{\mathrm{FE}} - \left(\frac{F}{A_0}\right)_i^{\mathrm{Exp}}\right]^2} \tag{21}$$

where N denotes the number of comparison points. Accordingly, the calibrated critical porosity is defined as

$$f_c^{\mathrm{cal}} = \arg\min_{f_c}\left[\mathrm{RMSE}(f_c)\right] \tag{22}$$

The effect of the critical porosity on the response of the R_6 specimen is shown in Figure 6(a). Lower values of f_c lead to earlier void coalescence and a more rapid loss of load-carrying capacity, whereas increasing f_c delays the onset of post-peak softening. Based on the comparison with the experimental response, $f_c^0 = 0.15$ was selected for the hydrogen-free material and was kept fixed during the subsequent hydrogen-dependent calibration.

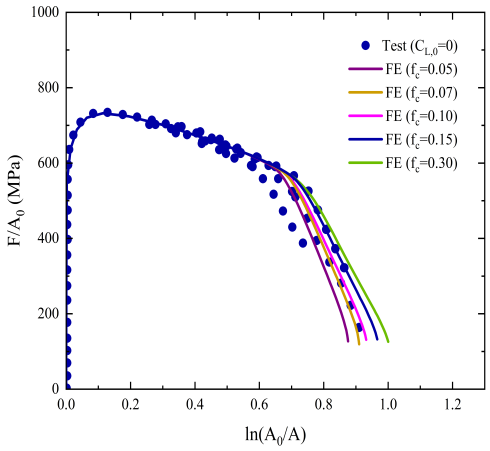
The responses are presented in terms of the normalised load F/A_0 as a function of the logarithmic area reduction $\ln(A_0/A)$. This representation reduces the influence of specimen dimensions and characterises deformation

through the local reduction of the minimum cross-sectional area, providing a consistent basis for comparing specimens with different notch geometries and constraint levels [50]. Accordingly, this representation is adopted for all numerical and experimental responses presented hereafter.

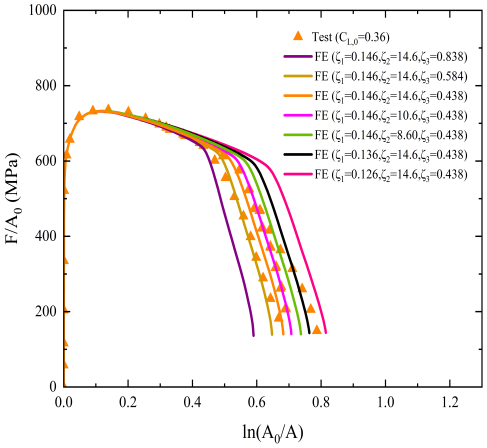
Once the hydrogen-free response was established, the remaining GTN parameters were kept fixed. The hydrogen-dependent parameters ζ_1 and ζ_2 in Equation 15 were initially identified using simulations at two different initial hydrogen concentrations. For each hydrogen condition, f_c was first varied independently without activating the proposed hydrogen-dependent critical-porosity relation until the corresponding experimental failure response was reproduced. The local lattice hydrogen concentration C_L at failure was then extracted from the FE analysis. The resulting pairs of C_L and f_c were substituted into Equation 15 to obtain initial estimates of ζ_1 and ζ_2. The parameter ζ_3 in Equation 16, which controls the hydrogen-dependent reduction in the ultimate void volume fraction, was subsequently determined from the post-coalescence response. During calibration, its numerical value was maintained as a percentage of ζ_2, and this percentage was adjusted to reproduce the experimentally observed post-coalescence response.

These initial estimates were subsequently refined using the fully coupled hydrogen–GTN simulations. The hydrogen-free parameters, including f_c^0 and f_f^0, remained unchanged, while the influence of ζ_1, ζ_2, and ζ_3 was examined against the hydrogen-charged experimental responses. Figures 6(b) and (c) show the corresponding sensitivity analyses for initial lattice hydrogen concentrations of $C_{L,0} = 0.36$ wppm and $C_{L,0} = 1.09$ wppm, respectively. Variations in ζ_1 and ζ_2 primarily influence the onset of the rapid load reduction by controlling the hydrogen-dependent critical porosity, whereas ζ_3 controls the reduction in the ultimate void volume fraction and therefore strongly influences the subsequent post-coalescence response and predicted failure deformation. The three parameters were progressively refined until a satisfactory description of both hydrogen-charged experimental responses was obtained.

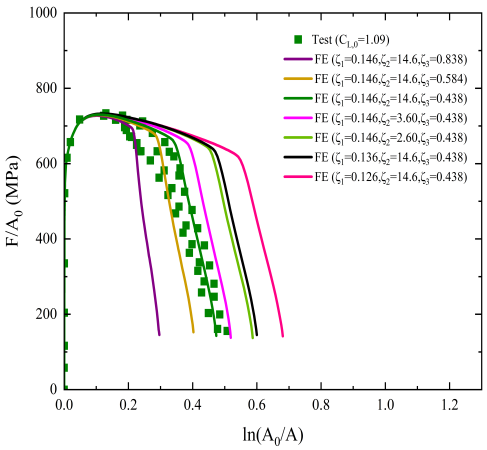
Following the assessment of the different parameter combinations, the values providing the best overall agreement with the hydrogen-charged experimental responses were selected as the final calibrated parameters. The resulting values are summarised in Table 2. For the material investigated in the present study, the degradation parameters were related to ζ_2 to reduce the number of independently calibrated parameters. Specifically, the numerical value of ζ_1 was taken as 1% of ζ_2, while $\zeta_3 = 0.03\zeta_2$. These relationships



(a) Calibration of $f_{c,0}$



(b) $C_{L,0} = 0.36$ wppm



(c) $C_{L,0} = 1.09$ wppm

Figure 6: Calibration of the hydrogen-free critical porosity f_c^0 and the hydrogen-degradation parameters ζ_1, ζ_2, and ζ_3 for the R_6 specimen: (a) identification of f_c^0 under the hydrogen-free condition and calibration of the hydrogen-dependent parameters at (b) $C_{L,0} = 0.36$ wppm and (c) $C_{L,0} = 1.09$ wppm.

are specific to the material and experimental conditions considered in the present study and have not yet been tested or validated for other materials. Although the exact parameter ratios may vary for different materials, the identified ratios are expected to provide a useful initial range for calibration, with subsequent adjustment according to the corresponding experimental response. The calibrated parameters were subsequently kept unchanged for the remaining specimen geometries and hydrogen conditions. Their predictive capability across different stress-triaxiality and hydrogen levels is assessed in the following section.

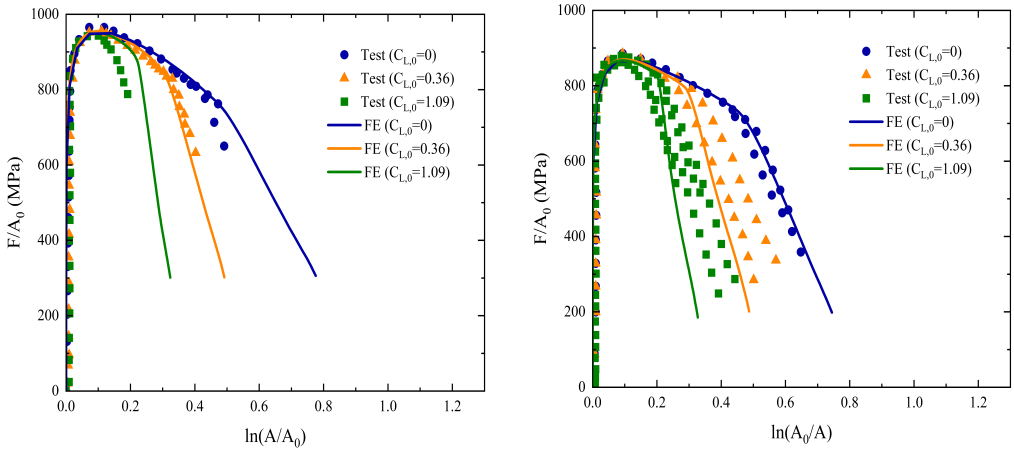
Table 2: Final calibrated parameters of the proposed hydrogen–GTN formulation.

Parameter	**Symbol**	**Value**
Hydrogen-free critical porosity	f_c^0	0.15
Degradation magnitude	ζ_1	0.146
Critical porosity degradation rate (wppm^{-1})	ζ_2	14.6
Ultimate porosity degradation rate (wppm^{-1})	ζ_3	0.438

4.2.2. Validation: transferability among different notch root radii

Following calibration using the R_6 specimen, the identified parameters were validated against the remaining specimen geometries to assess their transferability across different levels of stress triaxiality. All parameters listed in Table 2 were kept fixed, without further adjustment, and applied to the R_2, R_6, and R_∞ specimens under both hydrogen-free and hydrogen-charged conditions. The resulting numerical predictions are compared with the corresponding experimental responses in Figure 7.

As shown in Figure 7, increasing the initial hydrogen concentration generally reduces the deformation sustained before failure across the investigated specimen geometries. The proposed model captures this overall trend, although differences between the numerical and experimental responses are observed depending on specimen geometry and hydrogen concentration. For the $R_{1.2}$ specimen (Figure 7(a)), the hydrogen-free response is reproduced reasonably well, while the model predicts an earlier and more rapid load reduction under hydrogen-charged conditions, particularly at the higher hydrogen concentration. For the R_2 specimen (Figure 7(b)), good agreement is obtained for the hydrogen-free response, whereas the hydrogen-charged simulations predict an earlier onset of rapid softening than observed experimentally. A



(a) $R_{1.2}$ (b) R_2

(c) R_6 (d) R_∞

Figure 7: Comparison between the experimental and numerical responses for different specimen geometries and initial lattice hydrogen concentrations ($C_{L,0}$ = 0, 0.36, and 1.09 wppm).

similar behaviour is observed for the R_6 specimen (Figure 7(c)), although the agreement improves at the higher hydrogen concentration, where the predicted rapid load reduction more closely follows the experimental trend. For the smooth R_∞ specimen (Figure 7(d)), the hydrogen-free response is reproduced reasonably well. However, the hydrogen-charged simulations predict an earlier loss of load-carrying capacity than observed experimentally, particularly at the higher hydrogen concentration. Overall, the proposed model successfully captures the progressive reduction in ductility associated with increasing hydrogen concentration, although it generally overestimates the rate of hydrogen-induced degradation in terms of the predicted onset of rapid softening. These discrepancies highlight the influence of specimen geometry and stress triaxiality on the predictive accuracy of the proposed hydrogen-dependent formulation.

4.2.3. Accelerated Thomason-based model

To provide a consistent comparison with the proposed formulation (Equation 15), the accelerated Thomason coalescence criterion [51] was also considered. All material, GTN, and hydrogen-transport parameters listed in Table 1 were kept fixed without further calibration. Therefore, only the parameters governing hydrogen-induced degradation were calibrated. The hydrogen-dependent parameters k_{gL}, k_{nL}, η, and ξ of the formulation proposed by Depraetere et al. [24], defined in Equations 12, 13, and 14, were independently calibrated using the same hydrogen-charged experimental data employed for the proposed formulation. This procedure ensures that both approaches are compared using identical baseline material and hydrogen-transport properties, with the differences arising from their treatment of hydrogen-induced degradation and void coalescence. The resulting calibrated parameters are listed in Table 3.

Table 3: Calibrated parameters used in the Thomson method.

Parameter	**Symbol**	**Value**
Void-growth parameter (wppm^{-1})	k_{gL}	1.00
Void-nucleation parameter (wppm^{-1})	k_{nL}	1.20
Lower-bound parameter	η	0.80
Flow-stress degradation parameter	ξ	0.90

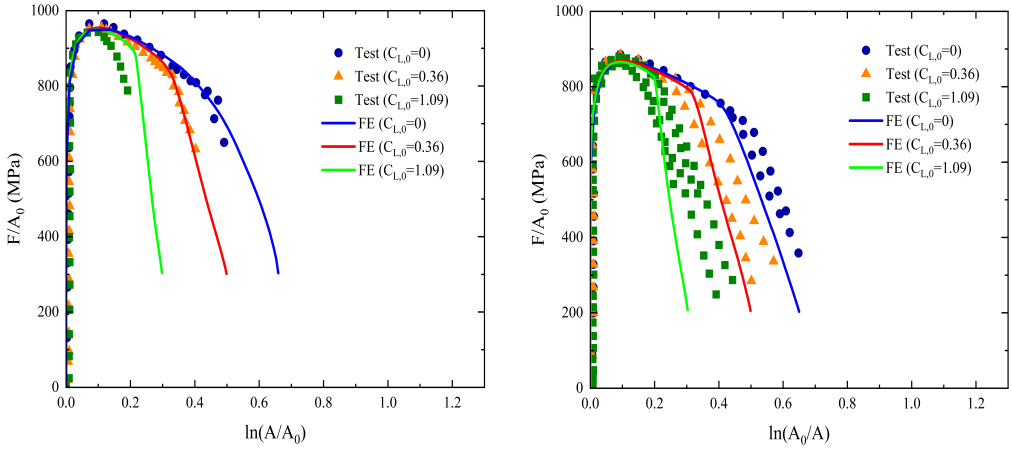
As shown in Figure 8, the predictive accuracy of the accelerated Thomason-based model varies with specimen geometry and hydrogen concen-

tration. For the $R_{1.2}$ specimen, the hydrogen-free response is reproduced reasonably well, while the model predicts an earlier onset of rapid load reduction under hydrogen-charged conditions, particularly at $C_{L,0} = 1.09$ wppm. For the R_2 specimen, good agreement is obtained under hydrogen-free conditions, whereas the hydrogen-charged simulations underestimate the deformation sustained before failure. This discrepancy becomes more pronounced at the higher hydrogen concentration. For the R_6 specimen, the hydrogen-free response is reasonably reproduced, while the model predicts a more rapid post-peak load reduction than observed experimentally for both hydrogen-charged conditions. The discrepancy is particularly evident at $C_{L,0} = 1.09$ wppm, where the predicted loss of load-carrying capacity occurs substantially earlier than in the experiments. For the smooth R_∞ specimen, the hydrogen-free response shows good agreement with the experimental measurements. However, the hydrogen-charged simulations predict an earlier onset of rapid softening, particularly at the higher hydrogen concentration. Overall, the accelerated Thomason-based model captures the general trend of decreasing ductility with increasing hydrogen concentration. Nevertheless, it tends to predict premature softening and failure under hydrogen-charged conditions, with the magnitude of the discrepancy depending on specimen geometry.

5. Discussion

Both models describe ductile fracture through void evolution and coalescence, but incorporate hydrogen differently. In the present model, hydrogen directly reduces the critical and final porosities through $f_c(C_L)$ and $f_f(C_L)$, while the conventional GTN void nucleation and growth relations remain unchanged. In the accelerated Thomason-based model, coalescence is instead determined by the Thomason criterion, with hydrogen affecting the constitutive response involved in this criterion. Therefore, the two models may reproduce similar macroscopic degradation while exhibiting different internal damage evolution.

In both models, crack initiation occurs at the central element of the specimens. The porosity values were therefore extracted from this element for the R_6 specimen to compare the underlying damage responses. Table 4 presents the porosity values at coalescence and final failure under hydrogen-free and hydrogen-charged conditions. In the present model, the coalescence porosity corresponds to $f_c(C_L)$, whereas in the Thomason-based model, it represents the porosity at which the Thomason coalescence criterion is satisfied.



(a) $R_{1.2}$ (b) R_2

(c) R_6 (d) R_∞

Figure 8: Comparison between the experimental and numerical responses obtained using the Thomson method for different specimen geometries and initial lattice hydrogen concentrations ($C_{L,0} = 0$, 0.36, and 1.09 wppm).

Table 4: Critical and ultimate void volume fractions predicted by the present model and the Thomason-based model for the R_6 specimen.

$C_{L,0}$ (wppm)	Present model		Thomason model	
	f_c	f_f	f_c	f_f
0	0.1570	0.4332	0.0498	0.4308
0.36	0.0047	0.3814	0.050	0.4367
1.09	0.0041	0.2890	0.053	0.4398

The results show that hydrogen strongly reduces the critical porosity in the present model, causing coalescence to initiate after substantially less void evolution. The relatively small difference in f_c between the hydrogen-charged conditions reflects the saturation behavior of the proposed relationship. In contrast, the final porosity continues to decrease with increasing hydrogen concentration, indicating a progressive reduction in the post-coalescence deformation capacity as formulated in the current proposal.

The accelerated Thomason-based model exhibits a different response, with both the coalescence and final porosities remaining relatively insensitive to hydrogen concentration. Thus, although both formulations predict hydrogen-induced degradation at the macroscopic level, the evolution of the internal damage variables differs considerably between the two models.

Figure 9 provides further insight into the fundamental differences between the proposed hydrogen-dependent GTN formulation and the accelerated Thomason-based approach. Although both models reproduce the overall reduction in deformation capacity of the material, associated with hydrogen exposure, they predict distinct internal damage evolution and plastic dissipation paths.

Figure 9(a) compares the relationship between porosity and accumulated plastic volumetric strain predicted by the two models. In the present model, the hydrogen-free and hydrogen-charged curves approximately follow the same trajectory, and the hydrogen-free response of the accelerated Thomason-based model also closely follows these curves. Increasing hydrogen concentration does not alter the trajectory in the present model; instead, hydrogen reduces the coalescence and failure thresholds through $f_c(C_L)$ and $f_f(C_L)$, causing failure to occur at an earlier point along this trajectory. This behaviour is consistent with the formulation of the model, in which the

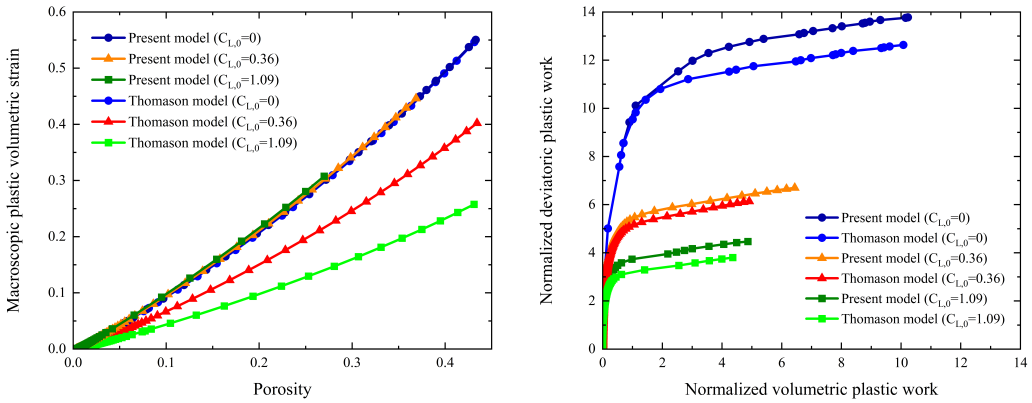


Figure 9: Comparison between the present model and the Thomason-based model for different initial lattice hydrogen concentrations $C_{L,0}$: (a) macroscopic plastic volumetric strain as a function of porosity; (b) normalised deviatoric plastic work as a function of normalised volumetric plastic work.

conventional void nucleation and growth relations remain unchanged.

In contrast, the accelerated Thomason-based formulation exhibits a progressively lower accumulated plastic volumetric strain for a given porosity as the hydrogen concentration increases. This behaviour reflects the hydrogen-dependent acceleration of void nucleation and growth introduced in the constitutive equations. Consequently, a larger amount of porosity can develop for a given macroscopic plastic volumetric deformation. Theese different trends therefore reflect the distinct hydrogen coupling and damage formulations of the two models.

It should also be noted that similar porosity—accumulated plastic volumetric strain relationships were observed for all specimen geometries. Although specimen geometry influences the local stress state and damage history, these differences become less apparent when porosity is plotted directly against accumulated plastic volumetric strain.

The comparison of plastic-work evolution in Figure 9(b) further highlights the different mechanical responses predicted by the two approaches. The deviatoric and volumetric contributions represent distinct components of the macroscopic plastic dissipation associated with distortional deformation and porous-material dilatation, respectively. Figure 9(b) compares the relationship between normalized deviatoric and volumetric plastic work for the R_6 specimen. Both quantities were normalized by the initial yield stress,

resulting in dimensionless measures of plastic work. All curves initially increase steeply and then gradually decrease in slope, indicating an increasing relative contribution of volumetric plastic deformation as damage develops. Increasing hydrogen concentration reduces both models, indicating a reduction in the plastic work accumulated during the damage process. Generally, the present model predicts greater accumulated deviatoric plastic work at a given volumetric plastic work than the accelerated Thomason-based model. This separation reflects differences in the internal damage evolution produced by the two formulations. While the present model introduces hydrogen-dependent coalescence and failure thresholds through $f_c(C_L)$ and $f_f(C_L)$, the accelerated Thomason-based model determines coalescence onset from the evolving stress, deformation, and hydrogen state. Together with the subsequent post-coalescence response, these differences result in different partitioning between deviatoric and volumetric plastic work, with a greater relative accumulation of deviatoric work in the present model.

The proposed hydrogen-dependent porosity formulation can also be discussed in the context of the Hydrogen-Enhanced Decohesion (HEDE) mechanism. HEDE attributes hydrogen-induced embrittlement to a reduction in the cohesive strength of material interfaces, thereby facilitating separation under tensile loading. Although the present formulation does not explicitly describe atomistic decohesion or introduce a hydrogen-dependent cohesive traction–separation law, the reduction in the critical porosity, $f_c(C_L)$, can be interpreted as a phenomenological representation of the reduced resistance of intervoid ligaments to coalescence. In this sense, hydrogen does not necessarily need to accelerate void nucleation or growth to promote premature failure; instead, it reduces the amount of void development that the material can sustain before the onset of accelerated coalescence. The additional reduction in the ultimate porosity, $f_f(C_L)$, further represents the loss of deformation capacity during post-coalescence damage evolution. This interpretation is consistent with the response illustrated in Figure 9 (a), where the hydrogen-charged simulations approximately follow the same porosity–plastic volumetric strain trajectory as the hydrogen-free case, but reach the coalescence and final failure conditions at earlier stages of deformation. Therefore, the proposed approach may be regarded as a continuum-level phenomenological description of hydrogen-assisted degradation of intervoid ligament resistance, potentially incorporating HEDE-related effects while preserving the conventional GTN formulation for matrix plasticity, void nucleation, and void growth.

6. Conclusions

A coupled hydrogen–GTN framework was developed to investigate hydrogen-assisted ductile failure in API 5L X70 pipeline steel. The Abaqus/Standard implementation incorporates hydrogen diffusion, trapping, stress-assisted transport, and ductile damage. Comparisons with reference crack-tip hydrogen distributions supported the verification of the transport formulation under transient and steady-state conditions. The main conclusions are:

- Hydrogen-induced reductions in deformation capacity can be represented through concentration-dependent critical and final porosities while retaining the conventional GTN void nucleation and growth laws and the hydrogen-independent matrix response. This provides a compact phenomenological approach to describing earlier coalescence and reduced post-coalescence deformation capacity.

- The calibrated critical-porosity relation approaches its lower limit under the investigated hydrogen-charged conditions. Consequently, the difference in coalescence porosity between the two charged conditions is relatively small, whereas the final porosity continues to decrease. The two thresholds therefore play distinct roles in controlling coalescence onset and subsequent failure.

- The model captures the overall hydrogen-induced reduction in deformation capacity across the notched specimens. Its applicability to the smooth specimen is more limited: although it reproduces the hydrogen-free response satisfactorily, it overestimates hydrogen-induced degradation for the case of an initial hydrogen equal to 0.36 ppm.

- The proposed and hydrogen-informed accelerated Thomason-based formulations predict different internal damage responses despite broadly similar macroscopic degradation trends. In the proposed model, the porosity–plastic volumetric strain curves follow a common trajectory, with hydrogen causing failure earlier. The accelerated Thomason-based formulation instead predicts concentration-dependent shifts in this relationship. These differences also produce distinct plastic-work partitioning, demonstrating that agreement with macroscopic tensile responses alone does not uniquely establish the underlying damage evolution.

- Hydrogen-induced embrittlement does not necessarily require an acceleration of macroscopic void growth. It may also be represented through a reduction in the critical resistance to void coalescence, leading to premature void failure along a different plastic deformation and dissipation path.

The results support hydrogen-dependent porosity thresholds as a practical phenomenological description of hydrogen-assisted ductile failure within the investigated conditions. Independent validation, particularly through local damage measurements and tests spanning additional constraint levels, hydrogen concentrations, and loading rates, is needed to establish the formulation's predictive range.

References

[1] Presidency of the Republic of Brazil, Legal framework for low-carbon hydrogen (2024).
URL https://www.planalto.gov.br/civil_03/_ato2023-2026/2024/lei/l14948.htm

[2] S. Thoudam, D. C. Ferreira, C. Ruggieri, D. F. Sarzosa, An elasto-plastic phase field framework for hydrogen-assisted failure with a stress-state-dependent critical fracture energy, Theoretical and Applied Fracture Mechanics 143 (2026) 105455. doi:10.1016/j.tafmec.2026.105455.

[3] K. Télessy, L. Barner, F. Holz, Repurposing natural gas pipelines for hydrogen: Limits and options from a case study in germany, International Journal of Hydrogen Energy 80 (2024) 821–831. doi:10.1016/j.ijhydene.2024.07.110.

[4] X. Fan, Y. F. Cheng, Hydrogen pipelines and embrittlement in gaseous environments: An up-to-date review, Applied Energy 387 (2025) 125636. doi:10.1016/j.apenergy.2025.125636.

[5] M. F. W. Chowdhury, C. V. Tapia-Bastidas, J. Hoschke, J. Venezuela, A. Atrens, A review of influence of hydrogen on fracture toughness and mechanical properties of gas transmission pipeline steels, International Journal of Hydrogen Energy 102 (2025) 181–221. doi:10.1016/j.ijhydene.2025.01.018.

[6] X. Li, Y. Zhong, H. Li, Y. Liu, G. Shan, D. Qu, J. Zhang, M. B. Djukic, Review of hydrogen embrittlement effect on fracture toughness of metallic materials: Influencing factors, and predictive models, Engineering Fracture Mechanics 327 (2025) 111392. doi:10.1016/j.engfracmech.2025.111392.

[7] M. Saneian, P. Han, S. Jin, Y. Bai, Fracture response of steel pipelines under combined tension and torsion, Thin-Walled Structures 154 (2020) 106870. doi:10.1016/j.tws.2020.106870.

[8] M. Saneian, P. Han, S. Jin, Y. Bai, Fracture response of steel pipelines under combined tension and bending, Thin-Walled Structures 155 (2020) 106987. doi:10.1016/j.tws.2020.106987.

[9] D. F. Sarzosa, M. Paredes, C. Ruggieri, Fracture prediction on hydrogen-charge notched samples using a stress-state-dependent phenomenological model, Engineering Fracture Mechanics 303 (2024) 110145. doi:10.1016/j.engfracmech.2024.110145.

[10] L. Jemblie, V. Olden, O. Akselsen, A coupled diffusion and cohesive zone modelling approach for numerically assessing hydrogen embrittlement of steel structures, International Journal of Hydrogen Energy 42 (16) (2017) 11980–11995. doi:10.1016/j.ijhydene.2017.02.211.

[11] S. Xenos, I. Papadioti, E. Kamoutsi, G. Haidemenopoulos, P. Sofronis, N. Aravas, Hydrogen embrittlement: Modelling material degradation and computational issues, Journal of the Mechanics and Physics of Solids 208 (2026) 106486. doi:10.1016/j.jmps.2025.106486.

[12] A. L. Gurson, Continuum theory of ductile rupture by void nucleation and growth: Part i—yield criteria and flow rules for porous ductile media, Journal of Engineering Materials and Technology 99 (1) (1977) 2–15. doi:10.1115/1.3443401.

[13] C. C. Chu, A. Needleman, Void nucleation effects in biaxially stretched sheets, Journal of Engineering Materials and Technology 102 (3) (1980) 249–256. doi:10.1115/1.3224807.

[14] V. Tvergaard, On localization in ductile materials containing spherical voids, International Journal of Fracture 18 (4) (1982) 237–252. doi:10.1007/BF00015686.

[15] M. Gologanu, J.-B. Leblond, J. Devaux, Approximate models for ductile metals containing non-spherical voids—case of axisymmetric prolate ellipsoidal cavities, Journal of the Mechanics and Physics of Solids 41 (11) (1993) 1723–1754. doi:10.1016/0022-5096(93)90029-F.

[16] M. Gologanu, J.-B. Leblond, J. Devaux, Approximate models for ductile metals containing nonspherical voids—case of axisymmetric oblate ellipsoidal cavities, Journal of Engineering Materials and Technology 116 (3) (1994) 290–297. doi:10.1115/1.2904290.

[17] V. Tvergaard, A. Needleman, Analysis of the cup-cone fracture in a round tensile bar, Acta Metallurgica 32 (1) (1984) 157–169. doi:10.1016/0001-6160(84)90213-X.

[18] M. Saneian, P. Han, Y. Zhang, Y. Bai, The hoop stress failure analysis of defective x80 steel pipes using damage mechanics models, Structures 90 (2026) 112260. doi:10.1016/j.istruc.2026.112260.

[19] D. F. Sarzosa, M. Verstraete, S. Hertelé, R. Denys, C. Ruggieri, Numerical simulation of ductile crack growth in medium wide plate specimens using 3-d computational cells, Engineering Fracture Mechanics 168 (2016) 26–45. doi:doi.org/10.1016/j.engfracmech.2016.09.008.

[20] A. Kumar, H. Singh, S. Haldar, R. Chhibber, Experimentally informed gtn model to predict ductile fracture in api x70 steel and weld using finite element analysis, International Journal of Pressure Vessels and Piping 219 (2026) 105633. doi:10.1016/j.ijpvp.2025.105633.

[21] T. Matsuo, J. Yamabe, S. Matsuoka, Effects of hydrogen on tensile properties and fracture surface morphologies of type 316l stainless steel, International Journal of Hydrogen Energy 39 (7) (2014) 3542–3551. doi:10.1016/j.ijhydene.2013.12.099.

[22] J. Yamabe, T. Awane, S. Matsuoka, Investigation of hydrogen transport behavior of various low-alloy steels with high-pressure hydrogen gas, International Journal of Hydrogen Energy 40 (34) (2015) 11075–11086. doi:10.1016/j.ijhydene.2015.07.006.

[23] H. Yu, J. S. Olsen, A. Alvaro, L. Qiao, J. He, Z. Zhang, Hydrogen informed gurson model for hydrogen embrittlement simulation,

Engineering Fracture Mechanics 217 (2019) 106542. doi:10.1016/j.engfracmech.2019.106542.

[24] R. Depraetere, W. De Waele, S. Hertelé, Fully-coupled continuum damage model for simulation of plasticity dominated hydrogen embrittlement mechanisms, Computational Materials Science 200 (2021) 110857. doi:10.1016/j.commatsci.2021.110857.

[25] Y. Deng, H. Liao, Y. He, Y. Yin, M. Pellegrini, G. Su, K. Okamoto, Y. Wu, Investigation on hydrogen embrittlement and failure characteristics of zr-4 cladding based on the gtn method, Nuclear Materials and Energy 36 (2023) 101463. doi:10.1016/j.nme.2023.101463.

[26] D. Lopes Pinto, A. El Ouazani Tuhami, N. Osipov, Y. Madi, J. Besson, Simulation of hydrogen embrittlement of steel using mixed nonlocal finite elements, European Journal of Mechanics - A/Solids 104 (2024) 105116, novel Developments in Mechanics of Materials - Special Issue on Occasion of Viggo Tvergaards's 80th Birthday. doi:10.1016/j.euromechsol.2023.105116.

[27] H. Yu, J. He, D. D. Morin, M. Ortiz, Z. Zhang, A self-consistent void-based rationale for hydrogen embrittlement, Scripta Materialia 255 (2025) 116403. doi:10.1016/j.scriptamat.2024.116403.

[28] T. Grossi, A. Guazzini, L. Romanelli, C. M. Belardini, B. D. Monelli, A multi-task bayesian optimization framework to identify a gurson–tvergaard–needleman constitutive model for an ms1500 steel in hydrogen environment, International Journal of Hydrogen Energy 248 (2026) 155696. doi:10.1016/j.ijhydene.2026.155696.

[29] S. A. Patil, S. Prüger, S. Roth, B. Kiefer, A finite element framework coupling chemo-mechanics and the non-local gurson–tvergaard–needleman model for hydrogen-induced ductility loss in steels, European Journal of Mechanics - A/Solids 118 (2026) 106121. doi:10.1016/j.euromechsol.2026.106121.

[30] D. Zhang, H. Zhang, Y. Yang, Y. Gong, Z. He, P. Chen, X. Liu, Development of a fracture damage constitutive model for high-grade steel pipeline girth welds in hydrogen environment, International Journal of

Hydrogen Energy 242 (2026) 155533. doi:10.1016/j.ijhydene.2026.155533.

[31] Z. Zhang, C. Thaulow, J. Ødegård, A complete gurson model approach for ductile fracture, Engineering Fracture Mechanics 67 (2) (2000) 155–168. doi:10.1016/S0013-7944(00)00055-2.

[32] M. Cauwels, R. Depraetere, W. De Waele, S. Hertelé, K. Verbeken, T. Depover, Effect of stress triaxiality on the hydrogen embrittlement micromechanisms in a pipeline steel evaluated by fractographic analysis, Materials Science and Engineering: A 886 (2023) 145689. doi:10.1016/j.msea.2023.145689.

[33] R. Oriani, P. Josephic, Equilibrium aspects of hydrogen-induced cracking of steels, Acta Metallurgica 22 (9) (1974) 1065–1074. doi:10.1016/0001-6160(74)90061-3.

[34] R. Oriani, P. Josephic, Equilibrium and kinetic studies of the hydrogen-assisted cracking of steel, Acta Metallurgica 25 (9) (1977) 979–988. doi:10.1016/0001-6160(77)90126-2.

[35] A. Krom, R. Koers, A. Bakker, Hydrogen transport near a blunting crack tip, Journal of the Mechanics and Physics of Solids 47 (4) (1999) 971–992. doi:10.1016/S0022-5096(98)00064-7.

[36] S. Larsson†, A. Carlsson, Influence of non-singular stress terms and specimen geometry on small-scale yielding at crack tips in elastic-plastic materials, Journal of the Mechanics and Physics of Solids 21 (4) (1973) 263–277. doi:10.1016/0022-5096(73)90024-0.

[37] M. Verstraete, W. De Waele, S. Hertelé, Development and validation of a high constraint modified boundary layer finite element model, International Journal of Sustainable Construction and Design 2 (2) (2011) 228–236. doi:10.21825/scad.v2i2.20520.

[38] G. Gobbi, C. Colombo, S. Miccoli, L. Vergani, A fully coupled implementation of hydrogen embrittlement in fe analysis, Advances in Engineering Software 135 (2019) 102673. doi:10.1016/j.advengsoft.2019.04.004.

[39] C.-S. OH, Y.-J. KIM, K.-B. YOON, Coupled analysis of hydrogen transport using abaqus, Journal of Solid Mechanics and Materials Engineering 4 (7) (2010) 908–917. doi:10.1299/jmmp.4.908.

[40] J. Besson, Continuum models of ductile fracture: A review, International Journal of Damage Mechanics 19 (1) (2010) 3–52. doi:10.1177/1056789509103482.

[41] R. Depraetere, W. De Waele, M. Cauwels, T. Depover, K. Verbeken, M. Boone, S. Hertelé, Influence of stress triaxiality on hydrogen assisted ductile damage in an x70 pipeline steel, Materials Science and Engineering: A 864 (2023) 144549. doi:10.1016/j.msea.2022.144549.

[42] M. Cauwels, R. Depraetere, W. De Waele, S. Hertelé, T. Depover, K. Verbeken, Influence of electrochemical hydrogenation parameters on microstructures prone to hydrogen-induced cracking, Journal of Natural Gas Science and Engineering 101 (2022) 104533. doi:10.1016/j.jngse.2022.104533.

[43] R. Depraetere, W. De Waele, M. Cauwels, T. Depover, K. Verbeken, S. Hertelé, Modeling of hydrogen-charged notched tensile tests of an x70 pipeline steel with a hydrogen-informed gurson model, Materials 16 (13) (2023). doi:10.3390/ma16134839.

[44] V. Diddige, S. Roth, B. Kiefer, Phase-field modeling of hydrogen-promoted fracture: Natural incorporation of hydrostatic stress dependencies via a chemical potential-based variational formulation, Computer Methods in Applied Mechanics and Engineering 445 (2025) 118143. doi:10.1016/j.cma.2025.118143.

[45] S. Nazar, H. Moradi, M. F. Milazzo, E. Proverbio, A coupled diffusion-kinetics model for hydrogen thermal desorption spectra from metals, International Journal of Hydrogen Energy 264 (2026) 156934. doi:10.1016/j.ijhydene.2026.156934.

[46] H. Maurya, F. Akhtar, Hydrogen embrittlement mitigation by surface modification: A review on current advances and future perspectives, International Journal of Hydrogen Energy 199 (2026) 152737. doi:10.1016/j.ijhydene.2025.152737.

[47] J. Faleskog, X. Gao, C. F. Shih, Cell model for nonlinear fracture analysis – i. micromechanics calibration, International Journal of Fracture 89 (1998) 355–373. doi:10.1023/A:1007421420901.

[48] T.-S. Cao, M. Mazière, K. Danas, J. Besson, A model for ductile damage prediction at low stress triaxialities incorporating void shape change and void rotation, International Journal of Solids and Structures 63 (2015) 240–263. doi:10.1016/j.ijsolstr.2015.03.003.

[49] T. Chai, R. R. Draxler, Root mean square error (RMSE) or mean absolute error (MAE)? – arguments against avoiding RMSE in the literature, Geoscientific Model Development 7 (3) (2014) 1247–1250. doi:10.5194/gmd-7-1247-2014.

[50] S. Tu, X. Ren, B. Nyhus, O. M. Akselsen, J. He, Z. Zhang, A special notched tensile specimen to determine the flow stress-strain curve of hardening materials without applying the bridgman correction, Engineering Fracture Mechanics 179 (2017) 225–239. doi:10.1016/j.engfracmech.2017.04.039.

[51] P. Thomason, Three-dimensional models for the plastic limit-loads at incipient failure of the intervoid matrix in ductile porous solids, Acta Metallurgica 33 (6) (1985) 1079–1085. doi:10.1016/0001-6160(85)90201-9.